Eur. Phys. J. D **62**, 5–17 (2011)
DOI: 10.1140/epjd/e2010-00271-8

THE EUROPEAN PHYSICAL JOURNAL D

Regular Article

How universal are Fibonacci patterns?

P.D. Shipman[1,a], Z. Sun[2], M. Pennybacker[3], and A.C. Newell[3,4]

[1] Department of Mathematics, Colorado State University, 80523-1874 Fort Collins, USA
[2] Department of Mathematics, University of California-Irvine, USA
[3] Program in Applied Mathematics, University of Arizona, USA
[4] Department of Mathematics, University of Arizona, USA

Received 22 May 2010 / Received in final form 18 August 2010
Published online 5 November 2010 –

Abstract. Pattern patterns, or phyllotaxis, the arrangements of phylla (flowers, leaves, bracts, florets) in the neighborhood of growth tips, have intrigued natural scientists for over four hundred years. Prominent amongst the observed features is the fact that phylla lie on families of alternately oriented spirals and that the numbers in these families belong to subsets $\{m_j\}$ of the integers defined by the Fibonacci rule $m_{j+1} = m_j + m_{j-1}$. The corresponding patterns, which we call Fibonacci patterns, are widespread and universal on plants. Our goal in this paper is to ask if they may also be seen in other physical structures and to try to quantify the circumstances under which one may expect Fibonacci patterns to occur.

1 Introduction

Patterns of an almost-periodic nature turn up all over the place. They appear as sandripples, as cloud formations, as granular cells on the sun's surface, and as the epidermal ridges on fingerprints [1,2]. In laboratories, they are seen in experiments on convection, on flame fronts, in chemical reactions, on compressed elastic shells, and on fat laser beams. They generally arise as instabilities when a system is driven far from equilibrium by some external stress. At some critical threshold, the uniform state becomes unstable and various shapes and configurations are preferentially amplified. The amplified configurations are rarely unique, reflecting remaining symmetries not broken at the point of instability. For the granddaddy of pattern-forming systems, convection in an infinite horizontal layer of fluid, the continuous translational symmetry is broken as the convecting motion breaks the fluid into cells with a preferred wavelength. But rotational symmetry is preserved and will only be broken by local biases. As a result, field variables $w(\vec{x}, t)$ such as the fluctuation temperature or vertical velocity can be written as a combination of sinusoidal shapes $\{a_j \cos(\vec{k}_j \cdot \vec{x} - \phi_j) f(z)\}$, where each wavevector $\vec{k}_j$ has a preferred length k_0 and $f(z)$ describes the vertical structure. The set $\{\vec{k}_j\}$ lies on a circle reflecting rotational symmetry. Each of the modes in this set can be thought of as a field of rolls (ridges, stripes) whose maxima lie on lines $\vec{k}_j \cdot \vec{x} - \phi_j = 2\pi n$ with normals $\vec{k}_j$ and distances $\frac{2\pi}{k_0}$ apart. Once the applied stress, here a nondimensional temperature difference, crosses the critical threshold, the individual modes grow and interact via nonlinearities. The winning configuration which emerges is called the winning, or chosen, planform. It is determined up to rotation and translation.

In many cases, the winning planform is either a field of rolls or hexagons. The reason hexagons have a special preference over, say, other $\vec{k}_j$ combinations such as squares is that, near onset, the strongest nonlinearity is quadratic as long as the system does not have an up-down $w \to -w$ symmetry. The quadratic product of two cosines $\cos(\vec{k}_1 \cdot \vec{x} - \phi_1)$ and $\cos(\vec{k}_2 \cdot \vec{x} - \phi_2)$ gives rise to cosines with wavevectors $\vec{k}_1 \pm \vec{k}_2$ and, in the absence of an up-down symmetry, the projection of $f^2(z)$ into $f(z)$ is nonzero. Generally, the generated wavevectors $\vec{k}_1 \pm \vec{k}_2$ do not lie on the critical circle of radius k_0. But, if $\vec{k}_1$ and $\vec{k}_2$ are 120° apart, then the resolved wavevector $\vec{k}_1 + \vec{k}_2$, also 120° apart in angle, has length k_0. The three shapes with wavevectors $\vec{k}_1$, $\vec{k}_2$, and the resolved wavevector $\vec{k}_1 + \vec{k}_2$ form a mutually interacting and reinforcing triad. If their amplitudes are equal, such a combination of modes gives rise to a field whose maxima lie on a perfect hexagonal lattice. The lack of up-down symmetry means that the convecting cells may have up- or down-welling at the field maxima, depending on the sign of the quadratic nonlinearity. If the amplitudes are different, they give rise to what we call imperfect hexagons. In the presence of the up-down symmetry, rolls are often preferred because the ratio of cross-coupling to self-coupling coefficients arising from cubic nonlinearities is greater than unity, and this makes configurations with a single field of rolls energetically more favorable. Because hexagons are more favored by quadratic terms but less favored by the cubic terms, there will generally be a transition from hexagon to roll states once the stress parameter exceeds the instability threshold by a sufficient amount so that the cubic interactions are more important

[a] e-mail: shipman@math.colostate.edu

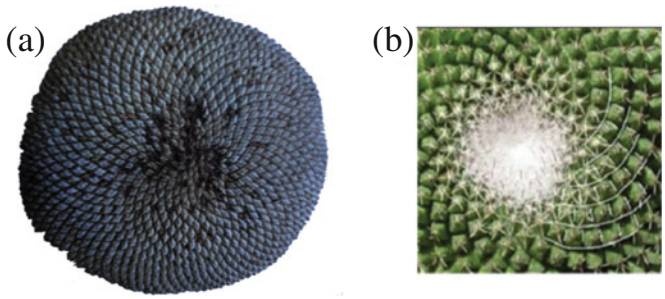

Fig. 1. (Color online) (a) A mature sunflower seed head displaying a Fibonacci pattern. At the outer edge, the pattern is dominated by families of 55 clockwise and 89 counterclockwise spirals. (b) A cactus showing the offset spirals; this structure is present, but not as apparent, in the sunflower.

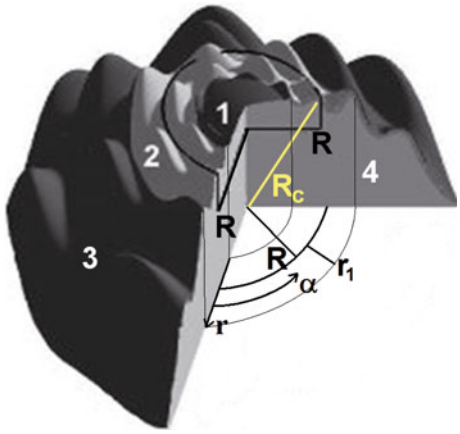

Fig. 2. (Color online) Diagram of the shoot apical meristem. In the regular process, cells are generated in region 1, the pattern forms in region 2-the *generative annulus*, and the primordia further develop into, for example, leaves as they move out to region 3.

than the quadratic ones. It is also important to include as active competitors all soft, or Goldstone, modes which may be present. They also reflect a symmetry inherent to the system. These modes, while neutrally stable or only very weakly damped, can be driven by quadratic DC interactions of the other amplified active modes. For example, the Oberbeck-Boussinesq equations are invariant under a constant change in the pressure field and, at low Prandtl numbers (namely, low viscocity), long-scale variations in the pressure field may be driven by long-scale variations in pattern intensity and affect in turn the choice of final configuration.

Once the winning planform has been chosen, its orientation, which, reflecting the original rotational symmetry, is still open, is chosen by local bias. For example, if rolls are the planform, then insulating (heated) lateral boundaries in the convection layer prefer rolls whose axes are perpendicular (parallel) to the boundary target. On fingertips, the epidermal ridges (rolls) prefer to align themselves so as to be parallel to the nail furrow or finger creases. In what we call natural patterns, the bias is different at different locations, and then the pattern consists of patches of almost straight rolls or almost perfect hexagons with different orientations which meet at and are mediated by point (convex and concave disclinations, dislocations) and line (phase and amplitude grain boundary) defects. If often takes a long time for such glassy-like states to coarsen to a minimum-energy configuration with one dominant orientation. Sometimes, as in one's fingertips, or, as we shall see, in plants, the pattern sets due to other influences which counterbalance the system's tendency to coarsen [2].

Patterns on plants, such as that observed on the sunflower head of Figure 1a, are, in many ways, like patterns in two-dimensional planar geometries. They form as quasiperiodic arrays of primordia (bumps) on the plant's surface near its shoot apical meristem (SAM) from which the phylla (leaves, florets, flowers, bracts) grow and mature. In many plants, these primordia lie on alternating clockwise and anticlockwise families of spirals and the numbers in each family are observed to belong to very special subsets of the integers called Fibonacci sequences. Observe such spirals on the sunflower head shown in Figure 1a. The plant surface-deformation field can be thought of as consisting of linear combinations of modes $\cos(l_j r - m_j \alpha)$, where r is the distance from the center of the SAM, α is the angular coordinate, and the integers m_j belong to Fibonacci sequences $\{m_j\}$ defined by the rule $m_{j+2} = m_j + m_{j+1}$. In contrast to planar patterns, the maxima of the field now lie on intersections of spirals $l_j r - m_j \alpha = 0 \pmod{2\pi}$. At any one radius, the pattern is dominated by a finite number of modes and alternates between what one can describe as rhombic and offset rhombic planforms. The former are essentially fields dominated by two wavevectors, and the latter by three. Because the amplitudes of the three modes in the latter case are not generally equal, they are imperfect hexagons and resemble spirals of rhombi in which neighboring spirals are offset by approximately 180° in phase; see Figure 1b. The radial and circumferential wavenumbers l_j, m_j have an associated length $k_j = \sqrt{l_j^2 + m_j^2/r^2}$ and, it turns out, for the dominant modes arising in the annular generative region with mean radius r (this is the region where primordia form, and the pattern is determined), this length is almost constant (k_0). Thus, just as was the case for patterns in planar geometries, there is a preferred wavenumber.

The differences between the planforms observed in what we call planar patterns and in plant patterns arise from the way in which they are formed. Planar patterns can form at roughly the same time over the whole domain depending on the presence of some local bias. Plant patterns form in a small annular region, called the generative region, at the outer boundary of the SAM, and they form annulus-by-annulus. We now describe the formation process.

The area near the apex of the SAM is divided into three regions, a central zone (region 1 in Fig. 2), containing what we call a mush of undifferentiated cells, a constantly renewed neighboring annular region where the skin, or tunica, of the plant has hardened and in which the region the primordia are generated, and an outer region

to which the primordia formed in what was previously a generative region have moved and where they mature into phylla. As a result of plant growth, a specific primordium, which is generated in region 2, will move radially outward into region 3, keeping its angular position fixed. In region 3, the primordia will continue to mature into fully developed phylla, but their angular positions remain unchanged. The pattern in region 3, modulo a radial shift due to growth, is frozen. Meanwhile, a new generative region forms behind it, and in it a new pattern is formed. Due to plant growth, the new generating radius will generally be at a larger distance from the apex than the old one. Therefore, because there is an intrinsic wavelength $\frac{2\pi}{k_0}$ associated with the emerging pattern, the circumference at which the new pattern is to be formed may accommodate a different set of modes with a different set of wavevectors. Central to the preference for Fibonacci patterns, the choice between various competitors for the new pattern will be heavily influenced by the bias and presence of the previously created pattern on the outer annular boundary between the new pattern and the previously formed pattern now in region 3. In this scenario, the pattern furthest away from the origin is the one with the least number of circumferential wavelengths and the circumferential wavenumbers of the phyllotactic pattern increase towards the apex. The wavevectors (l_j, m_j) of the dominant modes at the radius r are those modes preferred, not at r, but at the radius at which they were generated.

But, there is also a second scenario, which we call the sunflower scenario, in which the seeds or florets, the central part of the sunflower head, consists of patterns of spiral modes with circumferential wavenumbers belonging to Fibonacci sequences which decrease towards the plant apex. In this scenario, the pattern formed at the radius r stays at this radius. For this reason, the self-similar properties of Fibonacci patterns are much easier to see in the sunflower context. To understand this, we must learn how both the flower heads and florets of sunflowers arise. Here we outline the description given by Dosio et al. [3]. Sunflowers grow in two distinct stages. The first stage is the same as that for the first scenario. One can think of a top view of the new plants as consisting of two concentric circles. Both circles begin with zero radii. The circles move outward at different rates. The outer one, which we can associate with the plant size, moves more quickly than the inner one. Within the inner circle, which is called the meristem, the cells are undifferentiated and the plant material is more deformable. This is an area in which new tissue is created. Between the two circles, the surface, called the tunica, is more solid and can support stresses. It is in this area that primordia, or bumps, are initiated and eventually develop into elements such as leaves or the small flowers that make up the flower head of a composite flower, such as a sunflower or daisy, or bracts on a pinecone. At the initial stage of pattern formation, primordia form in pairs, giving what is called a decussate pattern. As the plant grows, the decussate pattern gives way to primordium positions which tend to fall on spirals which follow the Fibonacci sequence. At a certain point, after approximately 10 days, at which time the number of spirals in any of the families is fairly high up the Fibonacci sequence (in Fig. 1, the outermost spiral has 89 members), a new phenomenon occurs. The outer radius continues to grow, but the inner radius starts to shrink. At this point, the meristem produces a flower head, and the primordia mature into florets (which eventually give rise to seeds) rather than leaves. The meristem hole gradually disappears, and the flower head becomes filled with the primordia that develop into florets and then seeds. Shown in Figure 1a is a very mature sunflower head. The pattern was fully formed when the head was a couple of millimeters in diameter. From that planform and template, the head grew until it reached a diameter of about 20 cm. This growth is simply an isotropic rescaling of the pattern.

We note several very important properties of the final pattern of florets on the sunflower. First, and in contrast to the first scenario, the pattern stays where is is formed relative to the apex. In the first scenario, the pattern moves out due to plant growth. Second, and we will shall illustrate this property vividly in Section 3, it is self-similar, meaning that, under an appropriate transformation, the pattern at all radii is the same. Third, we note that the pattern becomes somewhat irregular close to the apex itself. This is to be expected. Basically, as one gets close to the center, there is simply not enough room either in the circumferential or radial directions for the intrinsic instability wavelength to fit. As a result, it is relatively rare to see spirals corresponding to the lowest members of the Fibonacci sequence expressed in sunflowers. Fourth, away from the central region, the pattern is optimal in the sense that it minimizes a functional which we shall call the free energy, formed by integrating the local free energy over an interval $(R, R\phi)$, where R is any radius, and $\phi = \frac{1}{2}(1 + \sqrt{5})$ is the golden number, the limit of successive integers in any Fibonacci sequence. Fifth, in a similar way, it maximizes, in a sense which we shall make precise, the packing efficiency of the seeds.

The regular scenario also give rise to patterns with optimal properties of free energy minima and packing density maxima, but only when defined using the measure of local area which pertains when the pattern is first formed. There is a possibly nonisotropic rescaling of the pattern as the annulus in which it formed moves away from the SAM and increases in size. This rescaling depends on the geometry of the plant head, which may vary from nearly a flat plane (as in the sunflower) to a hemisphere tapering down to a cylinder. In the remainder of this paper, we use the term optimal when referring to the property of the pattern when it is first laid down.

There are two main models which are used to understand these observations. Each has its strengths and weaknesses. The first is a paradigm based on a set of rules formulated by Hofmeister over one hundred and fifty years ago [4]. The key ideas are that primordia develop sequentially, one by one, and the position of each new one is chosen by being furthest away on the new circle (the center circle of the generative annulus) from all the ones formerly set down. For example, if distances between successive

circles are large enough, the angular position of each new primordium is 180° away from the positions of its immediate precursor. However, as the distance between the neighboring circles is reduced, the positions of the new primordia may depend on primordia laid down earlier. In an ingeneous experiment, and in a discrete-time dynamical system designed to follow these rules, Douady and Couder [5–7] showed how these rules give rise to arrays of primordia whose positions can be written as linear combinations of generating vectors and whose angular components are connected with Fibonacci sequences. A refined algorithm, based upon a revised set of Hofmeister rules by Snow and Snow [8], refined so as to allow for more than one primordium to develop at the same time, made possible the formation of deccusate and whorl patterns, in addition to Fibonacci patterns. In the Hofmeister algorithm, the lattice which results as a fixed point of the map can be described as a linear combination of two generating vectors obtained by joining each primordium to its two nearest neighbors. Let the nearest neighbors be formed m and n steps previously, where $m < n$. The integers m and n are called parastichies. The spirals formed by the two generating vectors wind in opposing directions around the circular region. As the distance between levels is changed, the distance between the new primordium and the one formed $m+n$ steps earlier becomes an equaldistant neighbor (as we will explain in the next section), and as the level is further reduced, becomes, with either m or n, one of the new parastichies. The consequence that parastichies give rise to opposingly oriented spirals means that the new parastichies are n and $m+n$. The two consequences of the class of Hofmeister maps, namely that the next candidate for being the nearest neighbor is $m+n$, and that the new parastichy pair is n, $m+n$, and not m and $m+n$, gives rise to Fibonacci sequences.

The strength of the paradigm is that it allows one to understand how a simple class of algorithms, each differing in detail but sharing key common features, can produce Fibonacci patterns. The weakness is that it does not explain how plants can use their physical and chemical properties to implement such an algorithm. We now describe a second approach which attempts to address this weakness.

This new approach, with which we have been most connected [9–15], attempts to build a model for phyllotaxis on the bases of the interconnected mechanisms of biochemistry and mechanics. The ideas stem from two sources. The first proposed mechanism was pioneered by Green et al. [16,17] and was based on the idea that differential growth in the plant's tunica could lead to compressive stresses sufficiently large to cause buckling in the generative region. The idea was then that at certain stress maxima, biochemical reactions triggered by stress inhomogeneities would lead to the formation of phylla at these locations. The second mechanism is based on the work of the labs of Smith et al. [18], Jönsson et al. [19] and de Reuille et al. [20] in the early part of this decade. Reinhardt et al. [21] had shown that the presence and absence of the hormone auxin had a powerful effect on the stimulation or inhibition of the formation of primordia. The question was: how might variations in auxin concentration occur naturally so as to provide sites for new primordia? In equilibrium situations, nonuniformities in chemical concentrations are smoothed out by diffusion. What the labs of Kuhlemeier and Meyerowitz showed, however, was that in the vicinity of the SAM, the situation was not an equilibrium one. Excess auxin in one cell relative to its neighbors triggered an action which sent a certain PIN1 protein from the cell interior to the cell walls where it oriented so as to pump auxin *with* its auxin gradient. This reverse diffusion effect, when sufficiently strong, can overcome ordinary diffusion and lead to instabilities and a natural quasiperiodic array of auxin concentration maxima and minima. This is precisely the ingredient one needs for preferential sites for primordium initiation.

We took advantage of the fact that the length scale $(\frac{2\pi}{k_0})$ of the auxin concentration variation was many cell diameters and replaced a cell-by-cell analytical description of auxin concentration interactions developed by Jönsson et al. [19] by a continuum model. It turns out that the resulting partial differential equation for the auxin concentration fluctuations has a canonical form associated with many pattern-forming systems. Near onset, namely near the value of the stress parameter which expressed the amount ϵ by which reverse diffusion exceeds ordinary diffusion, the equation takes the form

$$\frac{\partial g}{\partial t} = (\epsilon - (\nabla^2 + k_0^2)^2)g + \text{nonlinear terms}, \qquad (1.1)$$

which has the form of the Swift-Hohenberg equation familiar in pattern-forming systems.

Further, since it is well known that there is a strong coupling between stress and growth in living tissue, we included the mechanical stress fields so as the incorporate the ideas of Green et al. The growth strain $g(\vec{x}, t)$ resulting from fluctuations in auxin concentrations affects the stress field through the stress-strain relation. We modelled the effect of stress on growth (the fact that stress modifies growth is well known; how it does so has not yet been codified) by the simple idea that growth is induced when cells are under a tensile stress. We added a term proportional to the trace of the fluctuation stress tensor (the best measure of "pulling apart") to equation (1.1) for g. The coupled equations for the fluctuating surface deformation $w(\vec{x}, t)$ normal to the curved elastic shell which constitutes the plant's tunica and for the growth strain $g(\vec{x}, t)$ have very much the same form. For the buckling deformation $w(\vec{x}, t)$, the corresponding ϵ (ϵ_m) is the amount by which the compressive stress exceeds a critical threshold, and there is also a corresponding preferred wavelength $\frac{2\pi}{k_{0,m}}$. When the two preferred wavelengths k_0 and $k_{0,m}$ are nearly equal and ϵ and ϵ_m are near zero, the combination of effects leads to an enhanced instability. When one effect dominates, the other becomes a slaved variable.

The key messages of this paper are that, in certain circumstances, Fibonacci and whorl configurations are also a consequence of the solutions of pattern-forming PDEs. Moreover, *all* of the self-similar properties which

are consistent both with observations and with the outcomes of discrete dynamical system algorithms continue to obtain. The PDEs contain more information and an invariant associated with the amplitudes of the modes which are dominant at any location. The role of the key parameter of the discrete dynamical system, the distance between radial values at which primordia are laid down, is taken by the radial distance r from the apex of the plant's growth stem at which the pattern is formed. As we have said, unlike planar patterns, plant patterns form annulus-by-annulus, and the presence of one configuration created at a different value of r in the neighboring annulus affects the outcome in the pattern-forming annulus. We can model the evolving pattern formation as a front through which the unstable unpatterned state is invaded by a patterned state whose configuration is slowing changing, depending on the current front location. Equivalently, when we write the dynamics in terms of active mode amplitudes, we can model the local formation as an evolving minimum of some energy functional which moves continuously through some appropriately chosen parameter space.

The strength of this second approach is that it is based upon actual physical and biochemical mechanisms experienced by the plant. Indeed, it is very evident in recent work in the Meyerowitz laboratory that mechanical stresses are nonuniform in the neighborhoods of emerging primordia. Moreover, the parameters in the model equations derive form quantities which can be measured. The weakness of this approach is that the analysis uses a decomposition, the amplitude equations, for the fields g and w which is better suited to large domains and has to be interpreted as a frontal region in the pattern context.

The outline of this paper is as follows: we introduce in Section 2 some of the main features and properties of the discrete dynamical system designed to mimic the Hofmeister rules (for which whorls are not possible). We follow the work of Atela et al. [22,23] who propose and analyze a discrete-dynamical system in which the universal, geometrical and self-similar properties of the resulting patterns are easy to see. We write down formulae for the positions of all the primordia in the limit where the map has reached its fixed point configuration and all the primordia lie on a lattice. These points are integer linear combinations of two generating vectors, which join the newest pimordium to the two nearest primordia in the lattice, called the parastichies. These depend on the parameter y which measures distance between the levels at which primordia are laid down. We show how, as y decreases, the points move in such a way so that the new primordia follow the Fibonacci rule. Namely, at certain bifurcation values of y, $y_{m,n}$, the original parastichies are replaced by a new set. We then, after a suitable rescaling, introduce a normalized dual lattice, a lattice of directions. The points on this lattice also move with the parameter y, and we see how they, too, also follow a Fibonacci sequence. And this normalized lattice and its behavior as function of y gives us the connection with pattern-forming systems. The normalized dual lattice vectors turn out to be precisely the lattice of favored modes in the nonlinear competition between the active modes released at the instability. In Section 3, we capture precisely this correspondence. The governing equation we work with is a simple Swift-Hohenberg-like equation (3.4) (in contrast to previous work, in which we study systems of PDEs based on the mechanisms described above [11,12]). We show that the motion of the wavevectors as function of radial distance R from the apex corresponding to fixed points of the governing PDE matches the motion of the dual lattice in the discrete dynamical system, and we show how rhombic lattices play a role in both types of system. In the PDE system, however, the description is richer in that there is an additional parameter in the PDE approach, namely the amplitude, which weights each competing mode. The amplitude sequence moves, as a function of radial distance from the apex, in a self-similar manner, giving an additional amplitude invariant which we have discussed in [10,15]. In Theorems 1 and 2 of Section 3, we extend the results of [10,15] to derive the mappings (topological conjugacies between the systems of ODEs resulting from analysis of the PDEs) which give rise to self-similar properties of both the lattice and the amplitudes for all Fibonacci-like sequences. With the exception of the one involving amplitudes not present in the discrete description, these self-similar properties correspond to those derived by AGH. In all cases, we find that the golden number $\phi = (1+\sqrt{5})/2$, plays a central role. It is the ratio of the successive y values at which bifurcations from one set of parastichies to another take place and, we show in Figure 6 of Section 3, that it is the range $(R, R\phi)$ over which energy measures vary periodically. Since the PDE approach involves amplitudes as well as wavevectors, tracking the change in the pattern as R varies is complicated by the fact that in transitions from, from example, a $2, 3, 5$ pattern to a $3, 5, 8 = 3+5$ pattern, a mode with wavevector corresponding to $2 + 5 = 7$ potentially has a significant enough amplitude to change the course of the transition. In Figure 4 of Section 3, we map out normal (e.g. 2, 3, 5 transitioning to 3, 5, 8) and abnormal (e.g. 2, 3, 5 transitioning to 2, 5, 7) branches. In a final new contribution of Section 3, we allow the modes corresponding to $2, 3, 5, 7$ and 8 to compete near transitions and show that, although there does in fact exist an energy minimum corresponding to the abnormal branch, only the normal branch is accessible from previous configurations as the parameter R unfolds continuously. Thus suggests that, like in the discrete-dynamical system model, the formation of Fibonacci patterns from a PDE system relies on a continuous unfolding of the parameter R. Thus, although standard pattern-forming equations can give rise to Fibonacci patterns, the additional ingredient of the unfolding parameter is necessary.

2 The discrete dynamical system model

Many of the fascinating properties of phyllotaxis, including the connection with Fibonacci sequences, have intrigued natural scientists for over four hundred years. The botanist Wilhelm Hofmeister published one of the earliest

studies of meristems [4], in which he proposed the following heuristic for primordium formation:

- The meristem is axisymmetric.
- Primordia form in a generative annulus on the periphery of the apex.
- New primordia form at regular time intervals.
- Primordia move radially away from the apex.
- Each new primordium forms in the least crowded spot left by the existing primordia.

These rules provided the basis for almost all dynamical system models, although the fixed time periodicity was relaxed by Snow and Snow [8].

In a pioneering series of work, Douady and Couder [5–7] showed via experiments that an algorithm incorporating the Hofmeister rules gives rise to much of what was observed on plants. They designed a laboratory experiment in which uniform drops of ferrofluid were periodically dispensed at the center of an circular oil-filled dish. A radial magnetic field gradient caused the drops to experience an outward force, which resulted in radial motion away from the center. The drops were also mutually repulsive, so each drop moved into the least crowded spot. They found that by varying the time period between drops and the strength of the magnetic field, spirals corresponding to different members of the Fibonacci sequence were formed. A subsequent numerical simulation was used to refine their results.

More recently, a discrete dynamical system was proposed by Atela, Golé, and Hotton in order to put the Hofmeister rules in a more geometrical framework [22]. We now present a brief introduction to their model. The surface of the meristem may be approximated by the surface of a cylinder Z. We coordinatize the points p on Z by $p = (\alpha, h)$, where $\alpha \in (-\frac{1}{2}, \frac{1}{2}]$ is the angular coordinate divided by 2π, and h is the height, so that $0 \leq h < \infty$. The phase space for the dynamical system is the set of sequences of points $\{p_m = (\alpha_m, my) \ : \ m \in \mathbb{N}\}$ on the cylinder, where y is a fixed positive number called the *internodal spacing*, and $\alpha_m \in (-\frac{1}{2}, \frac{1}{2}]$. The points in any sequence represent the positions of primordia on the cylinder, each primordium residing at one level my. The primordium at p_m may be thought of as the mth-oldest primordium. The map T for the dynamical system, defined by its action on the elements of a sequence, is given by $T(\alpha_m, my) = (\alpha_m, (m+1)y)$. That is, the map moves each primordium up one level while having no effect on its angular coordinate. To complete the definition of the map, however, we need to determine the angular coordinate of the point $p_0 = (\alpha_0, 0y)$. The idea is that α_0 should be chosen so that p_0 appears in the "least crowded spot". The crowdedness of a spot can be quantified by the distance to the nearest primordium, so let $d(p_m, p_n)$ be the Euclidean distance on the cylinder between points p_m and p_n. The distance from a new primordium with angular coordinate α_0 to its nearest neighbor is given by

$$D(\alpha_0) = \min_{m>0} d(p_0, p_m). \tag{2.1}$$

Hofmeister's least crowded spot is given by the maximum of D over all angular coordinates α_0.

A main result of [22] is that, neglecting arbitrary rotation, regular lattices are asymptotically stable fixed points of this dynamical system. By a regular lattice on the cylinder Z we mean a set of points

$$L(x, y) = \{p_m = (mx - \Delta_m(x), my) \ : \ m \in \mathbb{N}\},$$

for a fixed number $x \in [0, 1)$ called the *divergence angle*, and where $\Delta_m(x)$ is the closest integer to mx, so that $-\frac{1}{2} < mx - \Delta_m(x) \leq \frac{1}{2}$. Two criteria are primarily responsible for the selection of fixed point lattices. Due to the fact that d is locally convex, the location of each new primordium is equidistant from two existing primordia. As a result, the fixed-point lattice is rhombic. Additionally, the location of each new primordium has an angular coordinate between the two nearest primordia. One says therefore that the lattice is opposed. It is therefore rhombic, opposed, regular lattices that are stable fixed points of the dynamical system.

It is also useful to introduce the concept of a parastichy. Parastichies are lattice points p_m and integer multiples thereof such that a line drawn to the newest primordium p_0 passes through no other points. The most visible parastichies are those which are formed by the points closest to p_1. For example, select the closest lattice point to p_0. Then select the closest lattice point that is not a member of the first parastichy. Taking $m < n$, this is a pair $\{p_m, p_n\}$ which forms a basis for the lattice. The values m and n are the parastichy numbers of the lattice.

We now present calculations based on [22] yielding quantities that will be used to compare with the PDE model in the following sections. In the remainder of this section, it is convenient to place the newest primordium p_0 at the origin and write the primordia $p_m = (mx - \Delta_m(x), my) = (\alpha_m, h_m)$ using complex notation as $z_m = \alpha_m + ih_m$. The parastichy basis $\{p_m, p_n\}$ for a lattice with parastichy numbers m, n corresponds to

$$z_m = \frac{-A}{nA - m}, \quad z_n = \frac{-1}{nA - m},$$

where $A = e^{i\theta}$ for some $\pi/3 \leq \theta < 2\pi/3$ that depends on the internodal spacing. There is a bifurcation point at $\theta = 2\pi/3$ where a third basis vector $z_{m+n} = z_m + z_n$ becomes as small as z_m and z_n. The requirement that the basis remain opposed selects the branch with parastichy numbers $n, m+n$. The internodal spacing at these points is given by

$$y_{m,n} = \frac{\sqrt{3}/2}{n^2 + m^2 + mn},$$

and the divergence angle is given by

$$x_{m,n} = \frac{mp + nq + 2(np + mq)}{2(m^2 + mn + n^2)},$$

where $p = \Delta_n(x)$, and $q = \Delta_m(x)$ (in fact, $pm - nq = \pm\gcd(m, n)$). For m, n in the Fibonacci sequence, this limits to $1/\phi^2$. The ratio of internodal spacing at consecutive members of the Fibonacci

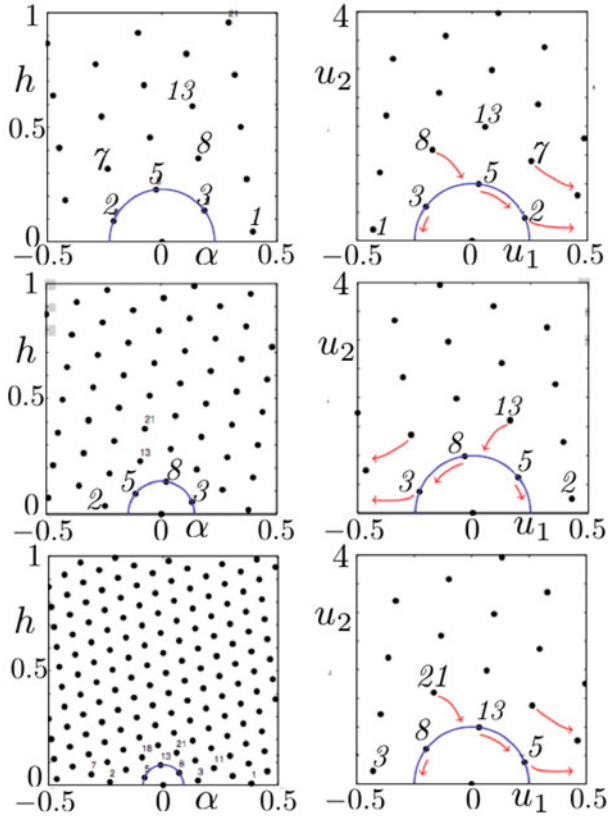

Fig. 3. (Color online) Fixed point lattices (left column) and corresponding normalized dual lattice vectors $\vec{u} = (u_1, u_2)$ (right column) for three transitions along the Fibonacci sequence as the internodal distance decreases. The lattices are shown for internodal spacings and divergence angles $y_{2,3}, d_{2,3}$ (top row), $y_{3,5}, d_{3,5}$ (middle row), and $y_{5,8}, d_{5,8}$ (bottom row). The half-circles in the right column are the unit half-circle.

sequence, namely

$$\frac{y_{n,m+n}}{y_{m,n}} = \frac{m^2+n^2+mn}{n^2+(m+n)^2+n(m+n)},$$

also limits to $1/\phi^2$.

In order to reveal a self-similarity in the pattern as y increases or decreases, we introduce normalized dual lattice vectors

$$\vec{u}_m = \frac{-\bar{z}_m}{|z_m|}, \quad \vec{u}_n = \frac{-\bar{z}_n}{|z_n|},$$

where $\{z_m, z_n\}$ is the parastichy basis, and $\bar{z}$ is the complex conjugate of z. These unit vectors are the directions of the parastichies reflected across the vertical axis. The reflection is performed so that these vectors correspond to the dual lattice vectors introduced in Section 3. For a rhombic lattice, $|z_m| = |z_n|$, and so for a general z_r we define $\vec{u}_r = z_r/|z_m|$. Figure 3 illustrates the fixed-point lattices and corresponding normalized dual lattices at three values of the internodal distance, namely the bifurcation values $y = y_{2,3}$, $y = y_{3,5}$, and $y = y_{5,8}$. In each case, the divergence angle used is the value $x_{m,n}$ that gives a rhombic (in this case, hexagonal) lattice. The arrows indicate the paths that each of the vectors take as the internodal spacing is decreased. The labels indicate the subscript corresponding to each vector. Note that the next member of the Fibonacci sequence is drawn toward the unit circle while the other pairwise sum is driven away. The normalized dual lattice is the same for $y = y_{2,3}$ and $y = y_{5,8}$, and a reflection of that lattice about the vertical axis yields the lattice at $y = y_{3,5}$.

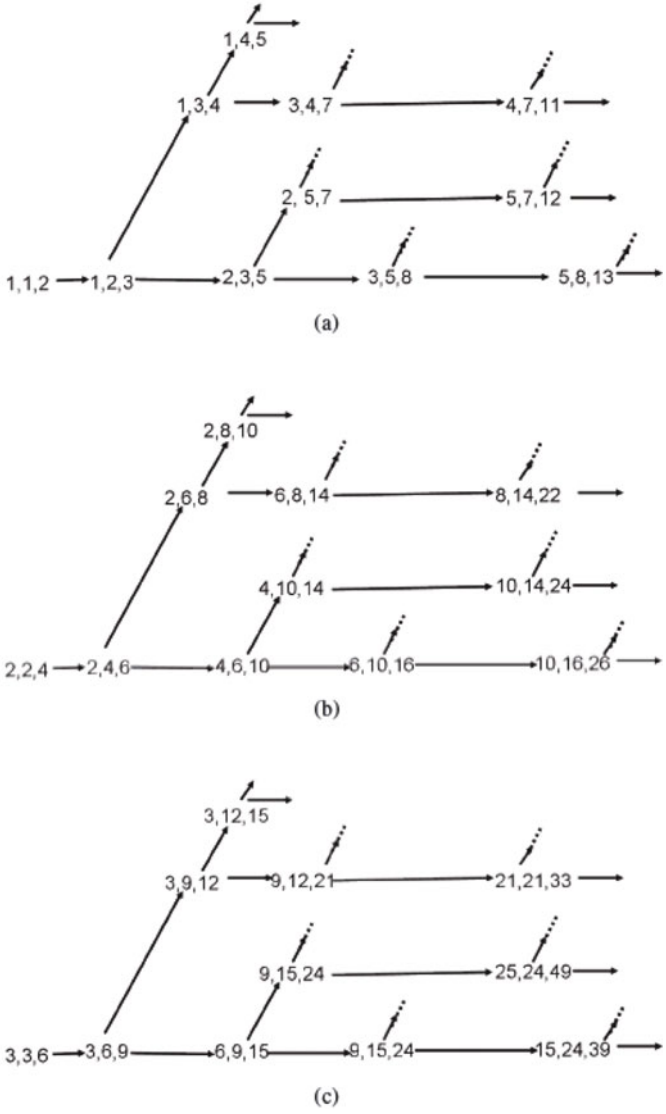

Fig. 4. (a) Family tree for the Fibonacci-like sequences with greatest common divisor 1. (b) Family tree for the Fibonacci-like sequences with greatest common divisor 2. (c) Family tree for the Fibonacci-like sequences with greatest common divisor 3.

In the PDE model with which we work in Section 3, the internodal distance is not a parameter, but must be determined by the solving the equations. The parameter that we can vary is the average radius R of the annular generative region where pattern formation is occurring. Increasing R will be analogous to decreasing the internodal distance. R, however, turns out to be approximately inversely proportional to the square of the internodal distance, or

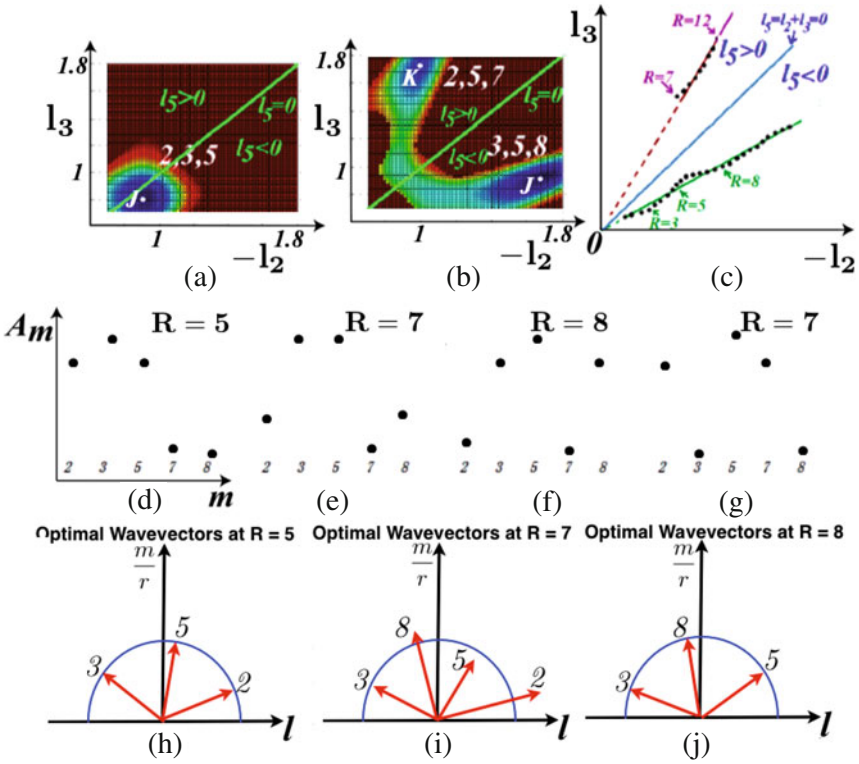

Fig. 5. (Color online) (a, b) The energy landscapes corresponding to the averaged energy (3.8) as functions of $-l_2$ and l_3 at (a) $R = 5$ and (b) $R = 8$. For $R = 5$, there is only one local minimum of the energy (marked by an J in (a)), whereas for $R = 8$, there are two local minima, marked by J and K in (b). For the minimum at J, $l_5 = l_2 + l_3$ is negative, whereas for the minimum at K, l_5 is positive. The loci of optimal radial wavenumbers corresponding to the two branches of energy minima are shown in (c) for a range of R values; linear approximations of the data points are plotted as well. The amplitudes corresponding to the energy-minimizing solutions are plotted in (d)–(f) for the minimum at J at $R = 5, 7, 8$ and in (g) for the minimum at K at $R = 7$. The energy-minimizing choice of wavevectors for the minimum at J are plotted in wavevector space in (h)–(i) for $R = 5, 7, 8$.

the plastochrone ratio [15]. The self-similarity that appears in the fixed-point lattices as the internodal distance y scales by $\frac{1}{\phi^2}$ will therefore manifest itself as a self-similarity in both lattices and amplitudes as R scales by ϕ in Section 3. The normalized dual lattice vectors of Figure 3 appear again in Figures 5h, 5j as the result of PDE calculations.

3 Order-parameter investigations

Our goal in this section is to translate the results described in Section 2 on bifurcations of a discrete dynamical system to the analysis of a PDE model. We first review our PDE model based on biochemical and biomechanical mechanisms, and we show how the model PDEs have the form of the Swift-Hohenberg equation. We then present an analysis of the simplified model equation (3.4) of Swift-Hohenberg type. As in our analysis of more complicated models, [11,13,14], we parameterize the space of possible configurations given by the solution $u(r, \alpha, t)$ of (3.4) by a set of order parameters that satisfy (after adiabatic elimination of spatial dependence) a gradient system of ODEs. The order parameters are a subset of the amplitudes and wavevectors in a Fourier representation of u, and this leading-order approximation of u allows for a center-manifold reduction of the dynamics. We then present two theorems on self-similarity as expressed in the reduced dynamics.

In [11], we formulate a system of PDEs governing the formation of plant patterns, based on biochemical and biophysical mechanisms as described in the introduction. The governing equations for the surface deformation w, the fluctuation f of the Airy stress potential, and the growth strain g have the following form:

$$w_t = -\Delta^2 w - \kappa w - \gamma w^3 - P\Delta_\chi w + \frac{1}{\nu}[f, w] - C\Delta_\rho f \tag{3.1}$$

$$\Delta^2 f - C\Delta_\rho w + \frac{1}{2\nu}[w, w] + \Delta g = 0 \tag{3.2}$$

$$g_t = -Lg - H\bigtriangledown^2 g - \bigtriangledown^4 g - \bar{\kappa}_1 \bigtriangledown (g \bigtriangledown g) - \bar{\kappa}_2 \bigtriangledown (\bigtriangledown g \bigtriangledown^2 g) - \delta g^3 + \beta\Delta f, \tag{3.3}$$

where $[f, w] = f_{xx}w_{yy} + w_{yy}f_{xx} - 2f_{xy}w_{xy}$. We refer the reader to [11] for details on the derivation and parameters; the key idea is that the Föppl-von Kármán-Donnell equations (3.1), (3.2) for a shell under stress P (where

$P > 0$ is compressive stress) are coupled to a continuum approximation (3.3) of the model of Jönsson et al. [19] for auxin transport, translated into equation for the growth strain g. It turns out that, near the onset of pattern formation where either or both the applied mechanical stress P (in (3.1)) or reverse diffusion H (the inverse diffusion induced by the polarized PIN1 transportation subtracted by the ordinary diffusion, in (3.3)) are close to their critical values, the pattern behavior is governed more by symmetries than by microscopic details. Accordingly, in order to gain a better understanding, we simplify this model so as to include the main ingredients. We recognize that equations (3.1) and (3.3) are both of Swift-Hohenberg type

$$\frac{\partial u}{\partial t} = -(\nabla^2+1)^2 u+\epsilon u+\vartheta(\nabla u)^2-2\vartheta\nabla(u\nabla u)-\gamma u^3 \quad (3.4)$$

where

$$\nabla^2 = \frac{1}{r}\frac{\partial}{\partial r}\left(r\frac{\partial}{\partial r}\right)+\frac{1}{r^2}\frac{\partial^2}{\partial\alpha^2}, \vec{\nabla} = \left\{\frac{\partial}{\partial r}, \frac{1}{r}\frac{\partial}{\partial\theta}\right\},$$
$$\nabla\cdot = \frac{1}{r}\frac{\partial}{\partial r}(r\cdot)+\frac{1}{r}\frac{\partial}{\partial\theta},$$

since their right-hand sides are composed of linear terms in the form $-(\nabla^2+1)^2+\epsilon$, quadratic nonlinear interactions and cubic saturations. The linear operator determines the optimal wavelength of the pattern and the optimal wavelength of w, g and u are $\frac{2\pi}{\sqrt{\frac{P}{2}}}$, $\frac{2\pi}{\sqrt{\frac{H}{2}}}$ respectively. The wavelength can be easily scaled to 2π (the wavelength of u), by rescaling the spatial coordinates. The nonlinearity determines the stable structures (rolls, hexagons, diamonds) out of many competing configurations. In the limit where the auxin induced instability is dominant and all mechanical variables w and f are slaved to g, the solutions to the coupled system (3.1)–(3.3) is primarily determined by equation (3.3) only without the coupling terms. Assume this is the case, and without causing qualitative change of the results, we replace the "real" governing equation (3.3) by equation (3.4). An advantage of equation (3.4) is that it is a gradient flow which minimizes the free-energy functional

$$\tilde{E} = \int\int\left\{\frac{1}{2}[((\nabla^2+1)u)^2-\epsilon u^2]-\vartheta u(\nabla u)^2 +\frac{1}{4}\gamma u^4\right\} r dr d\alpha \simeq \int E_r(r) r dr$$

where

$$E_r(r) = \frac{1}{2\pi r\triangle r}\int_{r-\triangle r/2}^{r+\triangle r/2}\left\{\frac{1}{2}[((\nabla^2+1)u)^2-\epsilon u^2] -\vartheta u(\nabla u)^2+\frac{1}{4}\gamma u^4\right\} r d\alpha. \quad (3.5)$$

Equally important as the form of the governing equations is the way that the patterns are formed. Instead of forming all at once on the entire large domain, the patternsform annulus-by-annulus, the established pattern serving as the boundary condition for the new pattern forming in an adjacent annulus. There may be many functions u that give local minima of the energy functional $\tilde{E}$, and the boundary condition selects from amongst these minima.

We take the following approach to approximating the propagation of the pattern as it minimizes the energy in each annulus: if the pattern first forms in an annular region of mean radius R_0, we break the space $(R_0,\infty)\times[0,2\pi)$ (or, $(0,R_0)\times[0,2\pi)$ for the sunflower seed head) into successive annuli with increasing (decreasing for the sunflower) effective mean radii $R_0, R_1, \ldots$ We first determine the active set and a winning configuration in the annulus of mean radius R_0. There may be multiple possible winning configurations, corresponding to local minima of the energy (3.5) reduced to a function $E(A_j,\vec{k}_j;R_0)$ for amplitudes A_j and wavevectors $\vec{k}_j$ of the active modes in a Fourier representation of u as described below, but biases will choose one minimum. We then unfold the energy $E(A_j,\vec{k}_j;R)$, allowing R to increase up the sequence $R_0, R_1, \ldots$ Again, there will be multiple minima at each value of R_j, but we mimic the generative front by finding the minimum at R_{j+1} that is accessible from the minimum at R_j.

To make the problem of finding energy-minimizing functions u tractable, we begin by representing u as a Fourier series. Our goal is to determine, as a function of R, the modes in this series that potentially dominate the pattern, and then to reduce the PDE to ODEs for the evolution of the amplitudes of these *active* modes. The remaining *passive* modes are slaved to the active modes in that they can be determined by algebraic functions of the active modes. How does one determine the active modes? First, we admit into this set modes with positive linear growth rates. Modes with slightly negative linear growth rates are also candidates for inclusion, as they may be important players in the dynamics due to nonlinear interactions with modes of positive linear growth. In particular, modes with wavevectors $\vec{k}_m = (l_m, m)$ and $\vec{k}_n = (l_n, n)$ in the active set interact via quadratic nonlinearities in the PDE with modes with wavevector $\vec{k}_m+\vec{k}_n \equiv \vec{k}_{m+n}$. (The wavevector $\vec{k}_m = (l_m, m)$ of any periodic mode consists of a radial wavenumber l_m, which can be any real number, and an angular wavenumber m, which is an integer.) Determining the separation between active and passive modes is complicated, however, by the fact that these sets may change with R. For example, although nonlinear interactions between the overlapping triads of wavevectors $\vec{k}_2+\vec{k}_3 = \vec{k}_5$ and $\vec{k}_3+\vec{k}_5 = \vec{k}_8$ may make it natural to include a mode with angular wavenumber 8 at small values of R, one also has to consider the possibility of a transition involving the wavevector triads $\vec{k}_3+\vec{k}_2 = \vec{k}_5$ and $\vec{k}_2+\vec{k}_5 = \vec{k}_7$.

The natural basis for systems with translational and rotational symmetries in circular geometries is the Hankel function basis $\{H_m^{\pm}e^{-im\alpha}\}$, where $H^{\pm}$ are the Hankel functions of the first and second kind. In terms of this

basis, the function u may be written as

$$u(r,\alpha,t) = \sum_{m\in\mathbb{N}} A_m^{\pm} H_m^{\pm}(k_m r) e^{im\alpha} + (*). \tag{3.6}$$

In the limit of large r and m, with fixed ratio m/r, the Hankel functions $A_m H^{\pm}(k_m r)$ may be approximated by $A_m^{s_m}(r,t)e^{i\int l_m dr}$, where $l_m = \sqrt{k_m^2 - m^2/r^2}$, and the superscript $s_m = \mathrm{sgn}(l_m)$. The decomposition of u is then approximated by

$$u(r,\alpha,t) = \sum_{m\in\mathbb{N}} A_m(r,t) e^{i\int l_m \mathrm{d}r - \mathrm{i}m\alpha} + (*), \tag{3.7}$$

where l_m and $m \in \mathbb{N}$ are the radial and circumferential wavenumbers of the Fourier modes, and the A_m are complex amplitudes. The superscript m describes the winding direction of the corresponding spiral family. If $l_m > 0$ (that is, $s_m = +$), the corresponding family of spirals winds counterclockwise; otherwise, it winds clockwise.

In the same limit, the Laplacian operator may be approximated by $\nabla^2 \simeq \frac{\partial^2}{\partial r^2} + \frac{1}{R^2}\frac{\partial^2}{\partial \alpha^2}$ (or, $\nabla^2 \simeq \frac{\partial^2}{\partial r^2} + \frac{1}{\Gamma^2}\frac{\partial^2}{\partial \alpha^2}$, where $\Gamma = \frac{R}{\Lambda}$ is the mean radius rescaled by Λ, and $2\pi\Lambda$ is the natural wavelength). Note that in making this approximation, we are assuming that R is very large compared to the natural wavelength. The radial range of the analysis is only a few pattern wavelengths; we will find below that the formation of Fibonacci patterns depends on a freezing of the older pattern behind the front edge. According to the linear terms of equation (3.4), the linear growth rate for a mode $A_m^{s_m}(r,t)e^{i\int l_m dr - im\alpha} e^{\sigma(l_m,m)t}$ is

$$\sigma(l_m,m) = -(k^2-1)^2 + \epsilon, \quad \text{where} \quad k^2 = l_m^2 + \frac{m^2}{R^2}.$$

For $\epsilon < 0$, $\sigma(l_m,m) < 0$ for all (l_m,m), but at $\epsilon = 0$ $\sigma(l_m,m) = 0$ for (l_m,m) on the circle (in $(l,\frac{m}{R})$-space) or ellipise (in (l,m)-space) $k^2 = 1$. For $\epsilon > 0$ there is an annulus of wavevectors around $k^2 = 1$ for which $\sigma(l_m,m) > 0$. The set $\mathfrak{A}$ of active wavevectors consists of those wavevectors (l,m), where m is an integer, and $\sigma(l,m) > \sigma^*$ for a small cutoff value $\sigma^* < 0$.

If we take the sum (3.7) over all wavevectors in $\mathfrak{A}$, and integrate the energy (3.5) over one generative annulus, we obtain an energy functional of the amplitudes and wavevectors of the active modes. The quadratic terms in the energy (corresponding to the linear terms in the PDE) give rise to terms of the form $A_m^{(*)}A_n^{(*)}e^{i(\pm\vec{k}_m \pm \vec{k}_n)}$, the integration of which over the annulus is zero except for those terms $A_m A_m^* e^{i(\vec{k}_m - \vec{k}_m)} = A_m A_m^*$. Similarly, the cubic terms in the energy (corresponding to the quadratic terms in the PDE) give rise to cubic products of the amplitudes. Those cubic products that do not integrate to zero are those of the form $A_m^* A_p A_q e^{i(\vec{k}_p + \vec{k}_q - \vec{k}_m)} = A_m^* A_p A_q$, where $\vec{k}_m = \vec{k}_p + \vec{k}_q$. Pairs of wavevectors $\vec{k}_p, \vec{k}_q \in \mathfrak{A}$ whose sum also lies in the active set interact via this nonlinear triad resonance and give rise to a cubic term in the averaged energy

$$E(\vec{k}\in\mathfrak{A}, A_{\vec{k}}; R) = -\sum \sigma(l_m,m) A_m A_m^* - \sum \tau_{mpq}(A_m^* \times A_p A_q + (*)) + \gamma \sum \left(\frac{1}{2}|A_m|^4 + \sum \delta_{mn}|A_m|^2|A_n|^2\right). \tag{3.8}$$

The quadratic and quartic terms in (3.8) are summed over all wavevectors $\vec{k} \in \mathfrak{A}$, and the cubic term in (3.8) is summed over all triads of wavevectors $\vec{k}_p, \vec{k}_q, \vec{k}_m = \vec{k}_p + \vec{k}_q$ in $\mathfrak{A}$. The coefficients $\sigma(l_m,m)$ (the linear growth rate), τ and γ are functions of the wavevectors and the parameters in the original energy functional. The center-manifold reduction of the PDE (3.4) is the gradient set of ODEs $\frac{\partial A_m}{\partial t} = -\frac{\partial E}{\partial A_m^*}$, the stationary solutions of which are minima of the energy (3.8).

But, although there is a finite set of possible values for the angular integer wavenumbers m, the corresponding radial wavenumbers l_m lie on continuous bands. Hence, there are still an infinite number of amplitudes included in (3.8), and our center-manifold reduction is an infinite system of ODEs. Experience with natural systems suggests that the dynamics reduces further to one or a few triads of modes in the active set. We restrict the dynamics to a set of modes with wavevectors $\vec{k}_1 = (l_1,1), \vec{k}_2 = (l_2,2), \vec{k}_1 + \vec{k}_2 = \vec{k}_3 = (l_3,3)$, and $\vec{k}_2 + \vec{k}_3 = \vec{k}_5$. The energy (3.8) thus simplifies to to an energy $E(A_1^{(*)}, A_2^{(*)}, A_3^{(*)}, A_5^{(*)}, l_1, l_2; R)$, and we find the optimal configuration by minimizing this energy with respect to the amplitudes A_m and the radial wavenumbers l_1, l_2. As discussed above, however, we need to understand why it is that the dynamics reduces to a set with angular wavenumbers $1, 2, 1+2 = 3, 2+3 = 5$ rather than to a set $2, 1, 2+1 = 3, 1+3 = 4$; or, to a set $2, 3, 5, 8$ rather than to a set $3, 2, 5, 7$.

In Figure 4, we map out possible transitions between triads of angular wavenumbers to produce family trees of Fibonacci-like sequences starting at various integer triads. Starting with the integer triad $1, 1, 2$, the standard Fibonacci sequence leads to successive triads $1, 2, 3$; $2, 3, 5$; ... by summing the second and third members of a triad to get the next triad in the sequence. At any point on this sequence, one may branch off by summing the first and last members of a triad. We will call the two types of branches the *normal* and *abnormal* branches, respectively.

Let us focus on the branching from a $2, 3, 5$ to either the normal $3, 5, 8$ or the abnormal $2, 5, 7$ branches as R increases. Without any a priori justification for including only modes with angular wavenumbers $2, 3, 5, 7$ or $2, 3, 5, 8$, we agree to include five modes with the angular wavenumbers $2, 3, 5, 7, 8$. Since $l_5 = l_2 + l_3, l_7 = l_2 + l_5$, and $l_8 = l_3 + l_5$, once we have chosen the angular wavenumbers, the energy is a function of the wavevectors only through l_2, l_3. We thus consider an energy $E(A_m, A_m^*, l_2, l_3; R)$, where $m \in \{2, 3, 5, 7, 8\}$. For any choice of l_2, l_3, we find the value of the amplitudes A_m that minimize $E(A_m, A_m^*, l_2, l_3; R)$, and plot the corresponding energy as a function of $(-l_2, l_3)$ in Figures 5a, 5b for $R = 5$ and $R = 8$. At $R = 5$, there is only one local

minimum of the energy, marked by a J in the figure. For this energy-minimizing solution, $-l_2 \simeq l_3$ and the amplitudes A_2, A_3, and A_5 are much larger than the amplitudes A_7, A_8. As we increase R from $R = 5$ up to $R = 8$, there is a continuous transition of this minimum to the position in $(-l_2, l_3)$-space marked by a J in Figure 5b. The corresponding amplitudes for this minimum also change continuously. As A_2 decreases, A_8 increases, while A_7 remains small. The amplitudes A_m at the minimum J are plotted in Figures 5d–5f for $R = 5, 7, 8$. For $R = 8$, there is a second minimum, marked by a K in Figure 5b. This second minimum first appears at $R = 6.5$ at a position in $(-l_2(h), l_3)$-space far removed from the original minimum (see Fig. 5c) and then moves continuously to the position shown in Figure 5b as R increases. The amplitude profile for this minimum at $R = 7$ is shown in Figure 5g; this minimum corresponds to a $3, 2, 5, 7$ pattern, as A_8, not A_7, is nearly zero. The key message of this calculation is that the normal $3, 5, 8$ transition branch is accessible from the $2, 3, 5$ pattern when R changes continuously, whereas the abnormal $2, 5, 7$ branch is not. The wavevectors for the normal transition are shown in Figures 5h–5j; notice that the wavevector $\vec{k}_7$ lies outside of the active set at $R = 8$.

This calculation shows that there is a family of solutions to the family of dynamical system parameterized by R that is dominated by modes with angular wavenumbers $2, 3, 5, 8$, the amplitudes and the optimal choice of (l_2, l_3) changing with R. The mode with angular wavenumber 7 consistently has an amplitude near 0, and as R increases, it moves further and further out of the active set, as seen in Figures 5h–5j. We may thus neglect it from the dynamics and capture the normal transition as R increases from 5 to 8 by an energy $E(A_m, A_m^*, l_2, l_3; R)$ for $m \in \{2, 3, 5, 8\}$.

Having examined the transition starting at the node $2, 3, 5$ in the family tree of Figure 4, we ask how our results apply at any other node in the tree; must we redo this calculation at each node? This question provides us with an opportunity to come back to the observations of Section 2. Notice that the wavevectors of Figures 5h, 5j are (approximately) the rhombic normalized dual lattice vectors of Figure 3 at $y = y_{2,3}$ and $y = y_{3,5}$ and recall that the key message of Figure 3 is the invariance of the lattice under the scaling $y \mapsto \frac{y}{\phi^2}$. We now show that, in fact, the dynamics at each node of Figure 4 is equivalent; in dynamical systems terminology, the gradient systems at all nodes are topologically conjugate. Geometrically, the equivalence comes from a self-similarity of the energy and the resulting energy-minimizing pattern under transformations of R and corresponding changes in the triads of angular wavenumbers.

The first key to understanding this self-similarity lies in noticing that the linear growth rate $\sigma(l_m, m)$ and the coefficients τ and γ in (3.8) only depend on the angular wavenumbers m and the radius R through the ratios $\frac{m}{R}$ appearing in the (squared) wavevector lengths $k^2 = l^2 + \frac{m^2}{R^2}$. Consider in light of this observation a simple example, energies $E_1(A_m, A_m^*, l_2, l_3; R_1)$ for $m \in \{2, 3, 5, 8\}$ and $E_2(A_n, A_n^*, l_3, l_5; R_2)$ for $n \in \{3, 5, 8, 13\}$. Written out more fully, we have $E_1(A_m, A_m^*, l_2, l_3; \frac{2}{R_1}, \frac{3}{R_1}, \frac{5}{R_1}, \frac{8}{R_1})$ and $E_2(A_n, A_n^*, l_3, l_5; \frac{3}{R_2}, \frac{5}{R_2}, \frac{8}{R_2}, \frac{13}{R_2})$, with corresponding minimizers $A_m(R_1)$, $l_2(R_1)$, $l_3(R_1)$ and $A_n(R_2)$, $l_2(R_2)$, $l_3(R_2)$, respectively. But, the second key to understanding self-similarity is that for any Fibonacci-like sequence $\{m_j\}$ defined by $m_{j+2} = m_j + m_{j+1}$, the sequence of fractions $\frac{m_{j+1}}{m_j}$ tends (quickly) to the golden number $\phi = \frac{1}{2}(1+\sqrt{5})$ for increasing j. If we take the approximation $\frac{3}{2} \simeq \frac{5}{3} \simeq \frac{8}{5} \simeq \frac{13}{8} \simeq \phi$ and choose $R_2 = R_1\phi$, then $\frac{2}{R_1} \simeq \frac{3}{R_2}$, $\frac{3}{R_1} \simeq \frac{5}{R_2}$, $\frac{5}{R_1} \simeq \frac{8}{R_2}$, and $\frac{8}{R_1} \simeq \frac{13}{R_2}$. We have (nearly) identical parameter values appearing after the semicolon in the energies E_1 and E_2, and therefore the energy-minimizing solutions are (nearly) identical; that is, $A_3(R_1\phi) \simeq A_2(R_1)$, $A_5(R_1\phi) \simeq A_3(R_1)$, $A_8(R_1\phi) \simeq A_5(R_1)$, and $A_{13}(R_1\phi) \simeq A_8(R_1)$. For the radial wavenumbers, $l_3^2(R_1\phi) \simeq l_2^2(R_1)$, and $l_5^2(R_1\phi) \simeq l_3^2(R_1)$. We should pause to consider the fact that the energy depends on the squares of the radial wavenumbers, and minimization by itself does not determine their sign. The stipulation that the sum $\vec{k}_2 + \vec{k}_3 = \vec{k}_5$, for example, lie in the active set, however, guarantees that $\mathrm{sgn}(l_2) = -\mathrm{sgn}(l_3)$. (This, by the way, is why we plot $(-l_2, l_3)$ in Fig. 5). The choice of the sign of l_2 then determines the (clockwise or counterclockwise) orientation of the corresponding family of spirals, and the spiral families have alternating orientations for increasing angular wavenumber. As R increases, the same orientation is chosen due to the accessibility of that minimum from the previous state.

More generally, let $\{m_j\}_{j=1}^{\infty}$ be a Fibonacci-like sequence of positive integers, and simplify (3.8) to a function

$$E\left(\{A_j\}_{j=1}^{\infty}, l_1, l_2; \left\{\frac{m_j}{R}\right\}_{j=1}^{\infty}\right) = -\sum_{j=1}^{\infty} \sigma\left(l_j, \frac{m_j}{R}\right) A_j A_j^* - \sum_{j=1}^{\infty} \tau(A_j^* A_{j+1} A_{j+2} + (*)) + \gamma \sum \left(\frac{1}{2}|A_m|^4 + \sum \delta_{mn} |A_m|^2 |A_n|^2\right) \quad (3.9)$$

of the variables $\{A_j\}, l_1, l_2$ and parameters $\{\frac{m_j}{R}\}$, where $l_{j+2} = l_j + l_{j+1}$. We want to find values of the variables that give a local minimum of E. The linear growth rate $\sigma = -(k^2 - 1)^2 + \epsilon$ that we have been considering will only be positive or slightly negative for a finite number of the $k_j^2 = l_j^2 + \frac{m_j^2}{R^2}$ (irrespective of the choices of l_j); as a consequence, only a finite number n of the amplitudes $A_\nu, \ldots A_{\nu+n}$ for some integer ν will be significantly larger than zero in a minimization, and we could consider the energy to be restricted to this finite set. Our observations lead to the following theorem:

Theorem 1. Suppose that the coefficients $\sigma(l_j^2, \frac{m_j}{R})$, $\tau(l_j^2, \frac{m_j}{R}, l_{j+1}^2, \frac{m_{j+1}}{R}, l_{j+2}^2, \frac{m_{j+2}}{R})$ and γ of the energy E given by (3.9) only depend on m_j and R through the ratios $\frac{m_j}{R}$. For a given value of R, suppose that $\{A_j(R)\}$, $l_1(R)$, $l_2(R)$ give a local minimum of E. Furthermore, suppose that $\{A_j(R)\}$ has finite support; for positive integers ν and n, $A_j(R) = 0$ for $j < \nu$ and $j > \nu + n$.

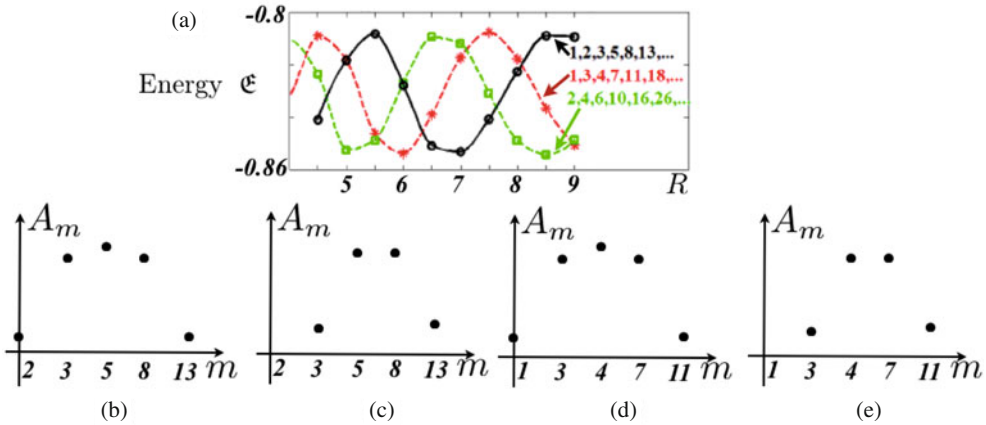

Fig. 6. (Color online) (a) Energy curves for three different Fibonacci-like sequences. (b–e) Amplitude curves for the regular Fibonacci sequence at (b) $R = 7$ and (c) $R = 9$, and for the Lucas sequence at (d) $R = 6$ and (e) $R = 9.5$. The similarities between (b) and (d), and between (c) and (e) are due to the one-to-one mapping between these two Fibonacci-like patterns (where $7/6 \simeq 9/7.5 \simeq 1.17$ is the asymptotical ratio between the regular Fibonacci sequence and the Lucas sequence).

Then, E is minimized by variables $A_{j+1}(R\phi) \simeq A_j(R)$, $l_2^2(R\phi) \simeq l_1^2(R)$, and $(l_3 = l_1 + l_2)^2(R\phi) \simeq l_2^2(R)$.

Proof. Replacing the parameters $\frac{m_j}{R}$ in $E(\{A_j\}_{j=\nu}^{\nu+n}, l_1, l_2; \{\frac{m_j}{R}\}_{j=\nu}^{\nu+n})$ by $\frac{m_{j+1}}{R\phi} \simeq \frac{m_j}{R}$, and renaming the variables A_j by A_{j+1} and (l_1, l_2) by (l_2, l_3), we obtain $E(\{A_j\}_{j=\nu+1}^{\nu+1+n}, l_2, l_3; \{\frac{m_j}{R\phi}\}_{j=\nu+1}^{\nu+1+n})$. •

As we do not have full equality in the statement $\frac{m_{j+1}}{R\phi} \simeq \frac{m_j}{R}$, one does need to provide estimates for a complete proof. However, the convergence of $\frac{m_{j+1}}{m_j}$ to ϕ is very quick, and the energy is a polynomial function of the amplitudes and wavevectors, so we do not provide the details here. This theorem may be generalized to a map between different Fibonacci-like sequences. Denoting the standard Fibonacci sequence by $\{f_j\}_{j=1}^{\infty}$, where $f_1 = f_2 = 1$, for any Fibonacci-like sequence $\{m_j\}_{j=1}^{\infty}$ generated by integers m_1, m_2, m_j may be written as $m_{j+2} = f_j m_1 + f_{j+1} m_2$. For any two Fibonacci-like sequences $\{m_j\}_{j=1}^{\infty}$ and $\{n_j\}_{j=1}^{\infty}$, therefore,

$$\frac{n_{j+2}}{m_{j+2}} = \frac{f_j n_1 + f_{j+1} n_2}{f_j m_1 + f_{j+1} m_2} = \frac{n_1 + \frac{f_{j+1}}{f_j} n_2}{m_1 + \frac{f_{j+1}}{f_j} m_2} \to \frac{n_1 + \phi n_2}{m_1 + \phi m_2} \equiv \phi_{mn}.$$

Hence,

$$\frac{m_j}{R} \simeq \frac{n_j}{R\phi_{mn}}.$$

Theorem 2. Consider two Fibonacci-like sequences $\{m_j\}_{j=1}^{\infty}$ and $\{n_j\}_{j=1}^{\infty}$ and corresponding energies $E_m \equiv E(\{A_j\}_{j=1}^{\infty}, l_1, l_2; \{\frac{m_j}{R}\}_{j=1}^{\infty})$ and $E_n \equiv E(\{B_j\}_{j=1}^{\infty}, l_1', l_2'; \{\frac{n_j}{R}\}_{j=1}^{\infty})$ given by (3.9). For a given value of R, suppose that $\{A_j(R)\}$, $l_1(R)$, $l_2(R)$ give a local minimum of E_m.

Then, E_n is minimized by variables $B_j(R\phi_{mn}) \simeq A_j(R)$, $l_1'^2(R\phi_{mn}) \simeq l_1^2(R)$, and $l_2'^2(R\phi_{mn}) \simeq l_2^2(R)$.

Proof. Replacing the parameters $\frac{m_j}{R}$ in $E(\{A_j\}_{j=\nu}^{\nu+n}, l_1, l_2; \{\frac{m_j}{R}\}_{j=\nu}^{\nu+n})$ by $\frac{n_j}{R\phi_{mn}} \simeq \frac{m_j}{R}$, and renaming the variables A_j by B_j and l_j by l_j', we obtain $E(\{B_j\}_{j=\nu}^{\nu+n}, l_1', l_2'; \{\frac{n_j}{R\phi_{mn}}\}_{j=\nu}^{\nu+n})$. •

This self-similarity is demonstrated in Figure 6. We calculate the amplitudes and radial wavenumbers that minimize the energy (3.9) restricted to finite sets of modes with angular wavenumbers in the normal Fibonacci sequence, the double-Fibonacci sequence $2, 2, 4, 6, \ldots$ and the Lucas sequence $1, 3, 4, 7, \ldots$ Also plotted in Figure 6a is the energy (3.9) as a function of R. We observe that the energy is not constant, but as a function of $\ln R$, it is periodic with period $\ln \phi$ regardless of the choice of Fibonacci-like sequence.

4 Conclusions

So, can we conclude that Fibonacci patterns are universal in the same way that many planar patterns are? What we have shown is that the fixed-point solutions of the broad class of algorithms are consistent with Hofmeister's ideas and that the adiabatic solutions of the order-parameter equations arising from a wide class of pattern-forming PDEs have certain universal features which would appear to resemble what is seen in plants. But, what we have not shown is that the energy minima discussed in Section 3 have large basins of attraction and can effectively complete with the many other local minima in the energy landscape. Indeed, direct simulations of the PDEs themselves seem to indicate that it is very easy for Fibonacci patterns to undergo Eckhaus-like instabilities and lead to textures which are part Fibonacci and part non-Fibonacci with many point (hepta-penta type) defects. The property that plants freeze their patterns once they are formed also seems to be very important.

Therefore, at this point in our investigations, we are not willing to claim that any pattern-forming system

which is dominated by quadratic nonlinearities and in which the pattern is laid down, annulus-by-annulus, by a generative front, will lead to Fibonacci patterns. We would claim, however, that if there were mechanisms to freeze the patterns in the wake of their formation, there would be open sets in parameter space (such as in the set of parameters determining the strength of the quadratic nonlinearity and front speed, the speed at which new generative annuli open up), for which Fibonacci patterns with all their self-similar properties would be the global attractor.

This work was supported by NSF Grant DMS-0906024 to ACN and NSF Grant DMS-0503196 to PDS.

References

1. M.C. Cross, H. Greenside, *Pattern Formation and Dynamics in Nonequilibrium Systems* (Cambridge UP, Cambridge, 2009)
2. M. Kuecken, A.C. Newell, Europhys. Lett. **68**, 141 (2005)
3. G.A.A. Dosio, F. Tardieu, O. Turc, New Phytol. **170**, 711 (2006)
4. W. Hofmeister, *Allegmeine Morphologie der Gewachse, Handbuch der Physiologischen Botanik* (Engelmann, Leipzig, 1868)
5. S. Douady, Y. Couder, J. Theor. Biol. **178**, 178 (1996)
6. S. Douady, Y. Couder, J. Theor. Biol. **178**, 255 (1996)
7. S. Douady, Y. Couder, J. Theor. Biol. **178**, 295 (1996)
8. M. Snow, R. Snow, Proc. Roy. Soc. B **139**, 545 (1952)
9. A.C. Newell, P.D. Shipman, J. Stat. Phys. **121**, 5 (2005)
10. A.C. Newell, P.D. Shipman, Analysis and Applications **6**, 4 (2008)
11. A.C. Newell, P.D. Shipman, Z. Sun, J. Theor. Biol. **251**, 421 (2008)
12. A.C. Newell, P.D. Shipman, Z. Sun, Plant Signal. Behav. **8**, 511 (2008)
13. P.D. Shipman, A.C. Newell, Phys. Rev. Lett. **92**, 168102 (2004)
14. P.D. Shipman, A.C. Newell, J. Theor. Biol. **236**, 154 (2005)
15. P.D. Shipman, Phys. Rev. E **81**, 031905 (2010)
16. P. Green, C. Steele, S. Rennich, Ann. Bot. **77**, 515 (1996)
17. P.B. Green, Am. J. Bot. **86**, (1999)
18. R.S. Smith, S. Guyomarc'h, T. Mandel, D. Reinhardt, C. Kuhlemeier, P. Prusinkiewicz, PNAS **103**, 1301 (2006)
19. H. Jönsson, M.G. Heisler, B.E. Shapiro, E.M. Meyerowitz, E. Mjolsness, PNAS **103**, 1633 (2006)
20. P.B. de Reuille, I. Bohn-Courseau, K. Ljung, H. Morin, N. Carraro, C. Godin, J. Traas, Proc. Natl. Acad. Sci. **103**, 1627 (2006)
21. D. Reinhardt, T. Mandel, C. Kuhlemeier, Plant Cell. **12**, 507 (2000)
22. P. Atela, C. Golé, S. Hotton, J. Nonlinear Sci. **12**, 641 (2002)
23. S. Hotton, Ph.D. thesis, University of California-Santa Cruz, 1999
24. A.H. Church, *On the Relation of Phyllotaxis to Mechanical Laws* (Williams and Norgate, 1904)
25. Z. Csahok, C. Misbah, Europhys. Lett. **47**, 331 (1999)
26. O. Hamant, M. Heister, H. Jönsson, P. Krupinski, M. Uyttewaal, P. Bokov, F. Corson, P. Sahlin, A. Boudaoud, E.M. Meyerowitz, Y. Couder, J. Traas, Science **332**, 1650 (2008)
27. S. Hotton, V. Johnson, J. Wilbarger, K. Zwieniecki, P. Atela, C. Golé, J. Dumais, J. Plant Growth Reg. **25**, (2006)
28. L. Pismen, A. Nepomnyashchy, Europhys. Lett. **27**, 433 (1994)